Power enhancement by increasing the initial array radius and wire number of tungsten *Z* pinches

C. Deeney, T. J. Nash, R. B. Spielman, J. F. Seaman, G. C. Chandler, K. W. Struve, J. L. Porter, W. A. Stygar, J. S. McGurn, D. O. Jobe, T. L. Gilliland, J. A. Torres, M. F. Vargas, L. E. Ruggles, S. Breeze, R. C. Mock, M. R. Douglas, D. L. Fehl, D. H. McDaniel, and M. K. Matzen
Sandia National Laboratory, MS-1194, Albuquerque, New Mexico 87185-1194

D. L. Peterson, W. Matuska, and N. F. Roderick*
Los Alamos National Laboratory, MS B-259, Los Alamos, New Mexico 87545

J. J. MacFarlane
Fusion Technology Institute, University of Wisconsin, Madison, Wisconsin 53706
(Received 4 October 1996; revised manuscript received 14 July 1997)

Tungsten wire array implosions on the 7- to 8-MA Saturn generator have been optimized using wire number and array diameter variations to produce 75 ± 10 TW of x rays with total energy outputs of 450 ± 50 kJ. By increasing the number of wires in a 12.5-mm-diam array from 24 to 70 and simultaneously decreasing the individual wire diameter from 13 to 7.5 μm, the total radiated power increased from 20 ± 3 to 40 ± 6 TW and the x-ray pulse width decreased from 18 to 8.5 ns. In addition, a diameter scan at an implosion time of 50 ± 5 ns showed that the pulse width has a strong dependence on collapse velocity and wire thickness. For the largest diameter load of 17.5 mm with 120 5-μm-diam wires, a 4-ns pulse width with a peak power of 75 ± 10 TW was achieved: four times power gain over the 20-TW electrical power generated by the pulsed power system. Time-resolved pinhole photography confirms that the power enhancement with increased wire number is associated with the plasma achieving a tighter compression and better axial uniformity. For the higher-velocity implosions, we infer from two-dimensional radiation-magnetohydrodynamic calculations that the plasma becomes hotter and hence radiates at a higher brightness temperature. Zero- and two-dimensional load models coupled with a detailed circuit model have shown expected radial kinetic energies in the range of 100–200 kJ. The total radiated energy of >400 kJ in a 4–20-ns FWHM pulse exceeds the total kinetic energy by more than a factor of 2. Two-dimensional, three-temperature simulations reproduce the observed trends in powers and pulse widths by using a variable initial random density perturbation. These calculations also indicate that the radiated energy is accounted for by the total work done on the plasma by the magnetic field. [S1063-651X(97)11111-4]

PACS number(s): 52.25.Nr, 52.65.−y, 52.55.Ez, 52.50.Lp

I. INTRODUCTION

Z pinches are very efficient at producing x rays ($>10\%$ conversion of stored electrical energy into x rays [1,2]). Unfortunately, they do not typically produce very high powers, which has limited their use for driving hohlraums, such as the laser-driven versions [3], for radiation and inertial-confinement-fusion applications. Attempts to increase the radiated power from *Z* pinches has been pursued previously, primarily for driving photo-pumped x-ray lasers [4–6]. With gas puff *Z* pinches, removing the zippering effect produced higher powers [7,8], and for metal elements, increased wire array number [9], foils [10], and mixtures [11], have all been observed to increase the radiated power. Most of this work has involved loads where the radiator was optimized for keV *K*-shell emission.

Theoretical [12,13] and experimental [14,15] efforts have been devoted to understanding the various scalings for *K*-shell radiators in the kilovolt regime, but there is less data on scaling of *L*-shell radiators [16] and very little on higher-atomic-number *N*- and *M*-shell radiators. In fact, the experimental database is limited to some low-current experiments with tungsten wire arrays [17] and then gold arrays [18] and some xenon implosions [19], including double-liner experiments with Xe [20]. The purpose of the experiments described below is to expand the database for high-atomic-number loads using tungsten wire arrays.

The experiments were performed on the 7-MA Saturn generator [19]; its parameters and the hardware plus diagnostics are described in Sec. II and the measurements of 40-wire, 12.5-mm-diam, 610-μm/cm tungsten implosions are discussed as an example in Sec. III. For the wire-number scan experiments described in Sec. IV, we chose to vary the number from 24 to 70 wires with the mass being held constant. The net effect of increasing wire number and decreasing wire thickness was to increase the radiated power by a factor of 2, as described in Sec. IV. In Sec. V, we describe experiments in which the wire array diameter is varied while the implosion times (approximately 50 ns) were held constant to study the effects of collapse velocity. The circumferential gap between adjacent wires was also held approximately constant at 0.5 mm. We observe that the higher

*Permanent address: Dept. of Chemical and Nuclear Engineering, The University of New Mexico, Albuquerque, NM 87131.

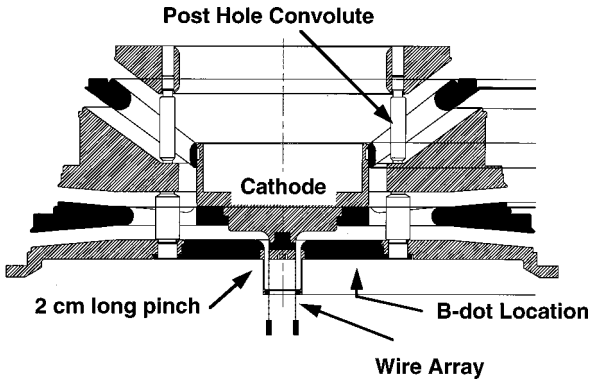

FIG. 1. Schematic of the four Saturn magnetically insulated transmission lines (*A* to *D*) feeding the post-hole convolute, and the wire array load region. Shielded *B*-dot current monitors are located in the radial MITL section 3 cm from the load. Diagnostics view the pinch at 35 degrees, so they see 12–14 mm out of the 2-cm pinch length. The wire array is strung between two stainless steel inserts which are positioned with the wires in the anode and cathode.

velocities reduce the x-ray pulse width to 4 ns, resulting in a peak x-ray power of 75 ± 10 TW. Furthermore, the combination of comprehensive soft-x-ray diagnostics plus new current monitors has determined that significant non-radial-kinetic heating must be occurring over the time scale of the pinch, which is described in Sec. VI along with two-dimensional (2D) radiation-magnetohydrodynamic modeling of the pinches. In Sec. VII, we discuss our conclusions and plans for future work.

II. THE SATURN GENERATOR AND DIAGNOSTICS

The experiments with tungsten wire arrays were performed on Saturn, which is a 36-module pulsed power generator [19]. Typically, Saturn delivers 8 MA beyond the insulator stack and 6.6 ± 0.2 MA into a small diameter (<20 mm) wire array load. Figure 1 shows the typical configuration used in this experiment. This figure shows the four magnetically insulated transmission lines (MITL feeds), the post-hole convolute that couples these lines into a radial feed. This radial-feed region then couples to the load region through a small coaxial section. The anode-cathode gap in this region is 3.75 mm (this gives 15% more energy coupling than a 2.5-mm gap would). The 2-cm-long wire array is mounted in two inserts that connect to the anode and cathode. Due to a combination of the hardware design and the 35 degree viewing angle of the ports, only 12–14 mm of the pinch was visible to the diagnostics. In Table I, we list the wire array configurations employed in the wire-number and radius scaling experiments discussed in this paper.

The generator is well suited to diagnose electrically and an accurate circuit model exists to calculate the effects of circuit and load modifications. In particular, calibrated 0.2-mil-thick NiCr shielded current probes are located 5 cm radially from the pinch: this current is called the feed current. These probes measure the local rate of change of the magnetic field (*B*-dot probes are integrated numerically to give current). The calibration procedure is accurate to $<2\%$ and involves inserting the *B* dots mounted in the actual anode hardware into a replica of the electrode structure that is fed by a known electrical pulse. Calibrated, multiple-shot *B* dots are also located in the separate MITLs upstream of the convolute; these measure the current injected past the insulator stack. The individual currents are averaged and then summed by level to give the total MITL current. Typically, the feed current is less than the total MITL current due to electron current losses in the MITLs and convolute region [21,22].

A set of x-ray diodes (XRD) [23] is our primary radiation diagnostic. There are four filtered vitreous-carbon-cathode [24] diodes with responses shown in Fig. 2: the filters are 4 μm Lexan, 1.5 μm titanium, 2.0 μm chromium, and 8 μm beryllium plus 1 μm of CH. Representative detectors were calibrated using a synchrotron facility. The filters are chosen to determine powers and radiation temperatures for the tungsten pinches which should have spectra similar to those shown in Fig. 3 at different temperatures (120, 160, and 200 eV). The spectra are dominated by broad transition arrays and continua as shown in Fig. 3(a), where unresolved-transition array (UTA) opacity calculations [Fig. 3(b)] are used with a local-thermodynamic-equilibrium (LTE) approximation to determine the emission spectrum [25]. The optical-depth plot in Fig. 3(b) is for a 160-eV, 1-mm-diam, 610-μg/cm pinch. At these opacities, the predicted spectra are about 85% of the energy of the equivalent blackbody at the same temperature. This gives credence to the three-temperature approximation employed in the two-dimensional radiation-magnetohydrodynamics (MHD) calculations in Sec. VI.

A gated, gold-photocathode microchannel plate (MCP) pinhole camera gave nine 100-μm, 100-ps space- and time-

TABLE I. List of the wire array configurations employed in the tungsten wire array scaling experiments along with the estimated kinetic energies, and the measured total radiated yields and pulse widths.

Load diameter (mm)	Load length (mm)	Wire no.	Wire gap (mm)	Wire thickness (μm)	Load mass (μg/cm)	Peak current (MA)	Implosion time (ns)	Collapse velocity (cm/μs)	Total radiated energy (kJ)	X-ray FWHM (ns)
12.5	20	24	1.63	13.0	614	6.6 ± 0.2	48 ± 3	50	450 ± 50	18 ± 2
12.5	20	40	0.98	10.0	606	6.6 ± 0.2	47 ± 2	50	450 ± 50	12 ± 2
12.5	20	70	0.56	7.5	612	6.6 ± 0.2	47	50	450 ± 50	8.5
7.0	17	40	0.55	18.0	2018	6.6 ± 0.1	46 ± 1	28	200	20 ± 2
12.5	20	70	0.56	7.5	612	6.6 ± 0.2	47	50	450 ± 50	8.5
7.5	20	120	0.46	5.0	450	6.4	45	65	530 ± 20	3.8 ± 0.2

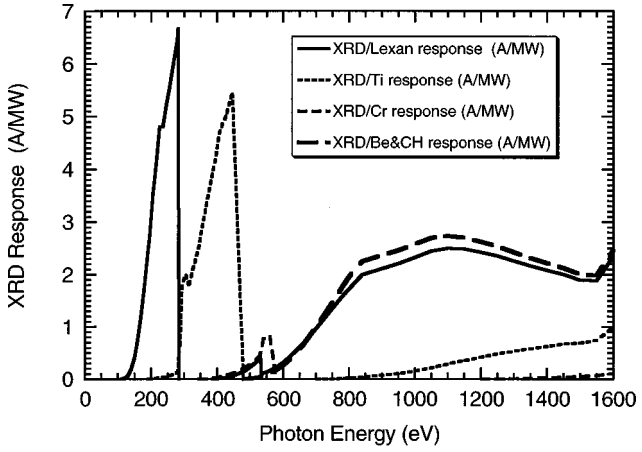

FIG. 2. Plot of the response functions of the four-channel, carbon cathode x-ray diode array employed to measure the emitted powers from the pinched plasma. The four filters are 4-μm Lexan, 1.5-μm titanium, 2-μm chromium, and 8-μm beryllium plus 1-μm Parylene_N.

resolved images of the pinch. This camera was filtered with 4 μm of Lexan. Another gated MCP camera has two time-integrated strips plus ten time-resolved strips, each with a 2-ns pulse duration, gated 3 ns apart. This camera has a magnification factor of 0.5 and is filtered with 8 μm of beryllium. These pinhole cameras are similar to those described in Ref. [26].

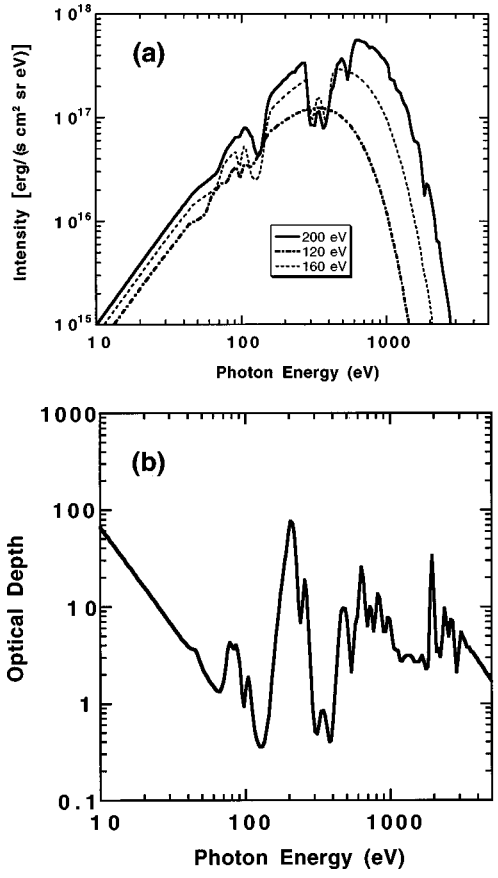

FIG. 3. (a) Calculated spectra for a 1-mm-diam, 610-μg/cm tungsten plasma with electron temperatures of 120, 160, and 200 eV are displayed. These calculations assume LTE and use opacities calculated by a UTA method. The optical depths for a 200-eV calculation is shown in (b).

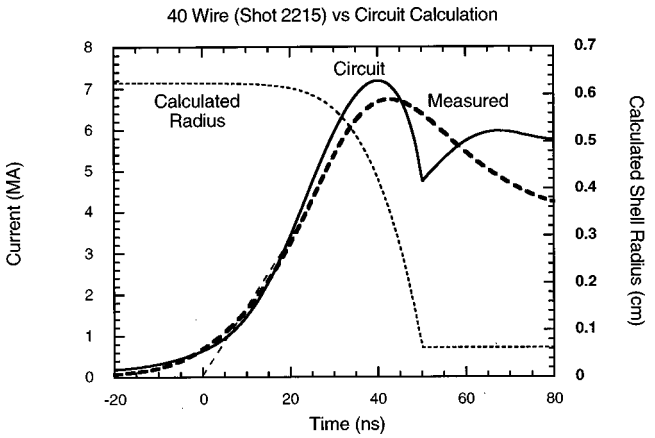

FIG. 4. Predicted currents and radius versus time for a 12.5-mm-diam, 610-μm/cm implosion. The measured feed current is shown as a dashed line for shot 2215. The circuit model used a vacuum flow impedance of 0.35Ω at the convolute. The extrapolated rise of the current to the baseline defines the start of the current pulse ($t=0$), as shown.

III. DYNAMICS OF A 610 μg/cm, 12.5-mm-diam ARRAY CONTAINING FORTY 10-μm-diam TUNGSTEN WIRES

Before discussing the radius and wire-number scans, it is instructive to look at the performance at one load condition. We have chosen the 610-μg/cm, 12.5-mm-diam, 40-wire tungsten array, since this configuration has the most data. In Fig. 4, we compare the zero-dimensional pinch dynamics (radius versus time) and currents predicted by the circuit model with the measured feed current. As mentioned in Sec. II, the feed current is less than the MITL current, i.e., 6.6 MA versus 8.0 MA. In addition, with the losses calculated adequately, the zero-dimensional model predicts the implosion time to within a few ns of the start of the x-ray pulse, where $t=0$ is defined by the extrapolated zero of the feed current. The circuit-model predicted implosion time is 50 ns; in the experiment, the x-ray pulse starts at 47 ns and peaks at 55 ns. The estimated kinetic energy is 160 kJ and the collapse velocity is 50 cm/μs from the circuit-model calculations, using the final compression (i.e., 10:1) determined from the $>$200-eV pinhole camera.

A summary of the different shots and load performance for the 40-wire arrays is given in Table II. Figure 5 shows the overlay of the MITL current, feed current (only 2215), and the total radiated power from three shots, which represent the extremes and average of all the shots taken. The total x-ray power is fairly reproducible from the 12 shots and is 27 ± 3 TW with a full width at half maximum (FWHM) of 13 ± 2 ns. The total radiated energy is 450 ± 50 kJ, which exceeds the kinetic energy by more than a factor of 2. Ohmic heating, pdV work due to instabilities, and many other processes could result in this additional energy deposition and thickening of the sheath. These will be discussed in a future paper.

The large-format time-resolved pinhole camera shows the

TABLE II. Summary of the measured parameters from the tungsten wire-number scan experiments. Clearly, as the number increases, the powers and brightness temperatures increase. In addition, the pinches become tighter and axially more uniform.

Wire no.	Peak power (TW)	Pulse FWHM (ns)	Kilovolt power (TW)	>200 eV peak power diam. (mm)	>200 eV peak power axial variation (mm)	>800 eV peak power diam. (mm)	>800 eV peak power axial variation (mm)	Radiation brightness temperature (eV)
24	17 ± 3	18 ± 2	2.0 ± 0.2	1.55 ± 0.03	16 ± 1	1.0	48 ± 3	115
40	32 ± 3	12 ± 2	3.0 ± 0.3	1.2 ± 0.1	20 ± 2	0.8	25 ± 2	140
70	40	8.5	5.5	0.9	20	0.7	20	160

stagnation dynamics. Figure 6 shows the frames recorded for a 40-wire-array shot. At around 48 ns, the initial thermalization is observed and the plasma has a typical axially averaged diameter of 0.9 ± 0.2 mm. From this point the plasma expands with a rate of about 6–10 cm/μs. By the time of peak power, the plasma has a diameter of 1.2 ± 0.1 mm. In Fig. 7, we show an example of the images from the standard-format pinhole camera that records >800-eV images. This camera has two time-integrated (marked T.I) images plus ten time-resolved images. The plasma diameter at peak power from this instrument is 0.77 ± 0.02 mm. The variation from shot to shot is less than the motional blurring, which should be no more 0.2 mm. For both cameras, the plasma diameter is determined by taking a length-integrated, radial lineout through the image, which is then fitted to a Lorentzian with a determined FWHM. Examples of peak-power radial profiles are given in Fig. 8. In Fig. 9, we show the axial variation of >800-eV x-ray emission (averaged over all radii) at peak power for a 40-wire shot. These show an axial variation of about $\pm25\%$ in intensity with wavelengths in the range of 0.5–2 mm. For the pinch diameter as illustrated in Fig. 8 and assuming the entire mass participates in the implosion, we infer an ion density of 2×10^{20} cm^{-3}.

On some shots, time-integrated spectral information has been recorded. Figure 10 depicts the measured spectrum from a 40-wire array. The spectrograph employed a curved potassium acid phthalate (KAP) crystal with film as the recording medium. The slope of the x-ray continuum, which is probably due to recombination into the *N* shell, is consistent with an electron temperature of <300 eV. The small edge at 1.5 keV is due to aluminum on the filter, which was not taken into account in the unfolding of the spectrum.

IV. RADIATED POWER VERSUS WIRE NUMBER FOR A 12.5-mm-diam ARRAY

By increasing the number of wires in the array, we increased the peak radiated power from the pinch. As the wire number increases, the wire separation decreases, as does the wire thickness if the mass is held constant. Figure 11 shows a comparison of the measured total radiated power plus total radiated energy from the 24-, 40-, and 70-wire arrays. The total radiated energies were 450 ± 40 kJ for all the wire arrays. The power pulses all have similar initial rises and drops but the peak moves earlier in the pulse. This would imply that the shell is becoming more well defined, since aluminum experiments [15] have indicated that the time of the peak power corresponds to a peak radiating mass on the axis for radiators with significant optical depths.

The enhancements in power were consistent with the decrease in pulse width, which is summarized in Fig. 12 as a function of wire-to-wire separation. The error bars reflect the shot-to-shot variation of typically $\pm10\%$. Clearly from Fig. 12, as the adjacent wire separation (gap) is decreased (i.e., wire number is increased) both the total radiated power and the kilovolt radiated power from the plasma increase and the pulse width decreases.

From Fig. 12, we see that the the ratio of the keV x-ray power to the total power increases for smaller wire separations. This is also substantiated by the spectral unfolding from the x-ray diode data. In Fig. 13, the power incident on the XRDs are shown for the four energy bins (as denoted by the data point and *x*-axis error bars) and for the different wire numbers. The *y*-axis error bars shows the spread in the measurements. As the wire number increases, the fractional power increase is higher for the higher-energy bins. Two explanations are possible: first, the plasma temperature could be increasing, or second, more mass is being heated. Since the implosion velocity should be almost the same for all the different wire numbers, it is less likely that the temperature increased; however, the time-resolved pinhole images do support the hypothesis that more mass is being uniformly heated.

Table II summarizes the analyses of the time-resolved pinhole images along with the power measurements. From this table, we observe that as the wire number increases, the ratio of the >200-eV plasma diameter to the >800-eV diameter decreases; the plasma diameters decrease; and the >800-eV axial uniformity improves. The generally increasing compression with increasing wire number is what one would expect from a more symmetric plasma stagnation. As the wire number increases, the magnetic field and hence mass is probably better confined radially (i.e., a thinner shell due to less magnetic field leakage), so that there is less preheated plasma on axis, as observed in the Al Mg experiments [11,27]. The increased ratio of the higher-energy emissions to the lower-energy emissions could be due to the higher densities resulting in an improved thermalization. This is akin to the improvements in power and yields, in aluminum, plasmas with increasing *K*-shell mass fraction [15].

The improvement in axial uniformity is less obvious, since the increased wire number improves azimuthal unifor-

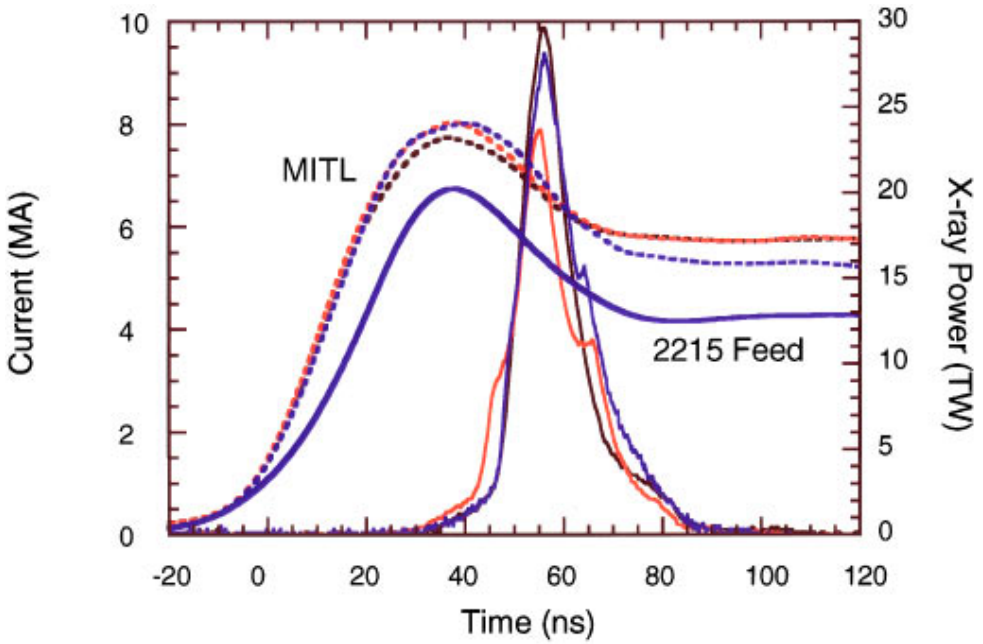

FIG. 5. (Color) An overlay of the measured MITL and feed currents with the measured x-ray powers from three 40-wire array implosions.

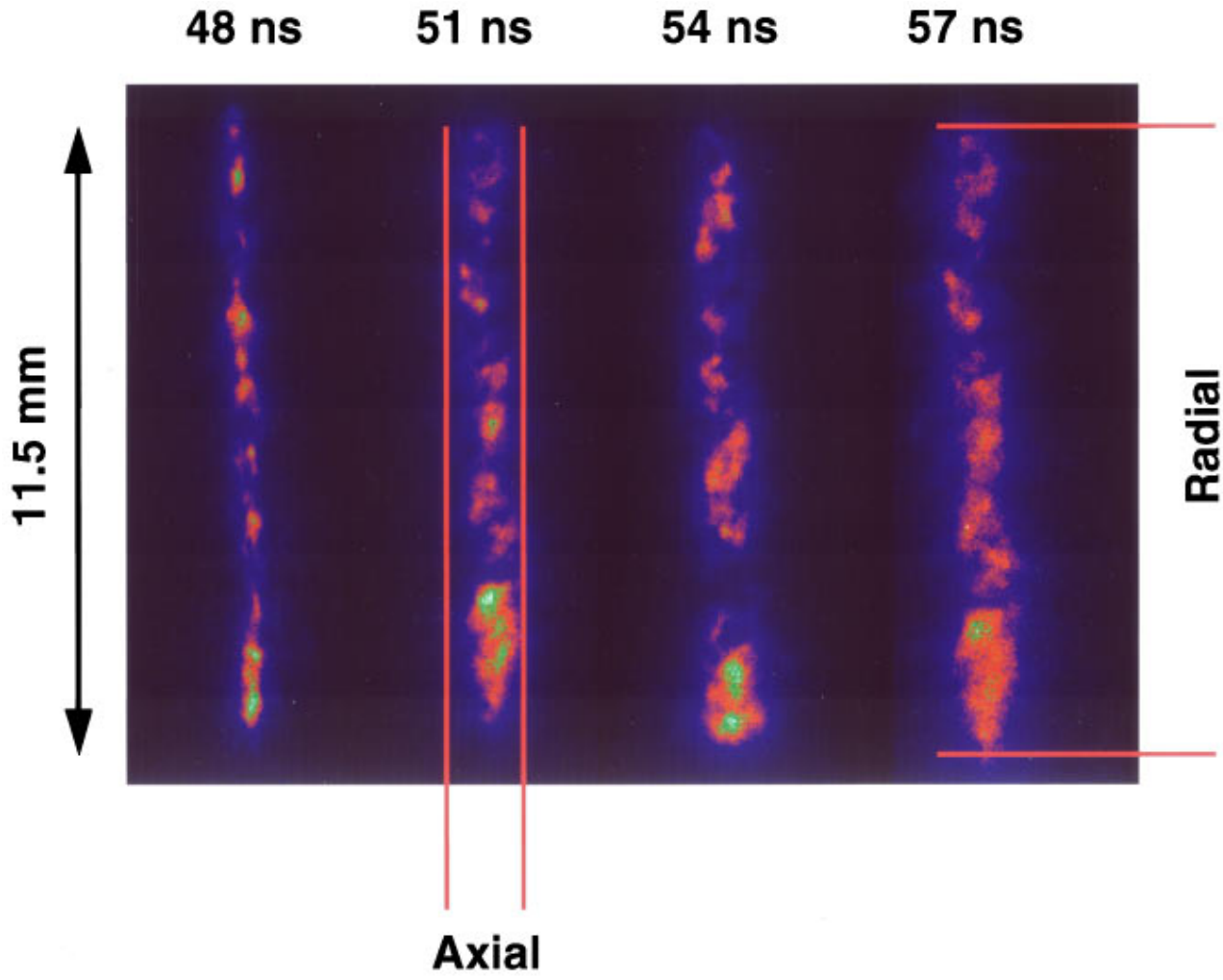

FIG. 6. (Color) Large-format images, with 100-ps temporal and 100-μm spatial resolution, of a 40-wire array implosion. This camera is filtered with 4 μm of Lexan and has a gold-coated microchannel plate. The times shown are relative to the extrapolated start of the current. The red parallel lines indicate the directions for axial and radial lineouts as shown in Figs. 8 and 9.

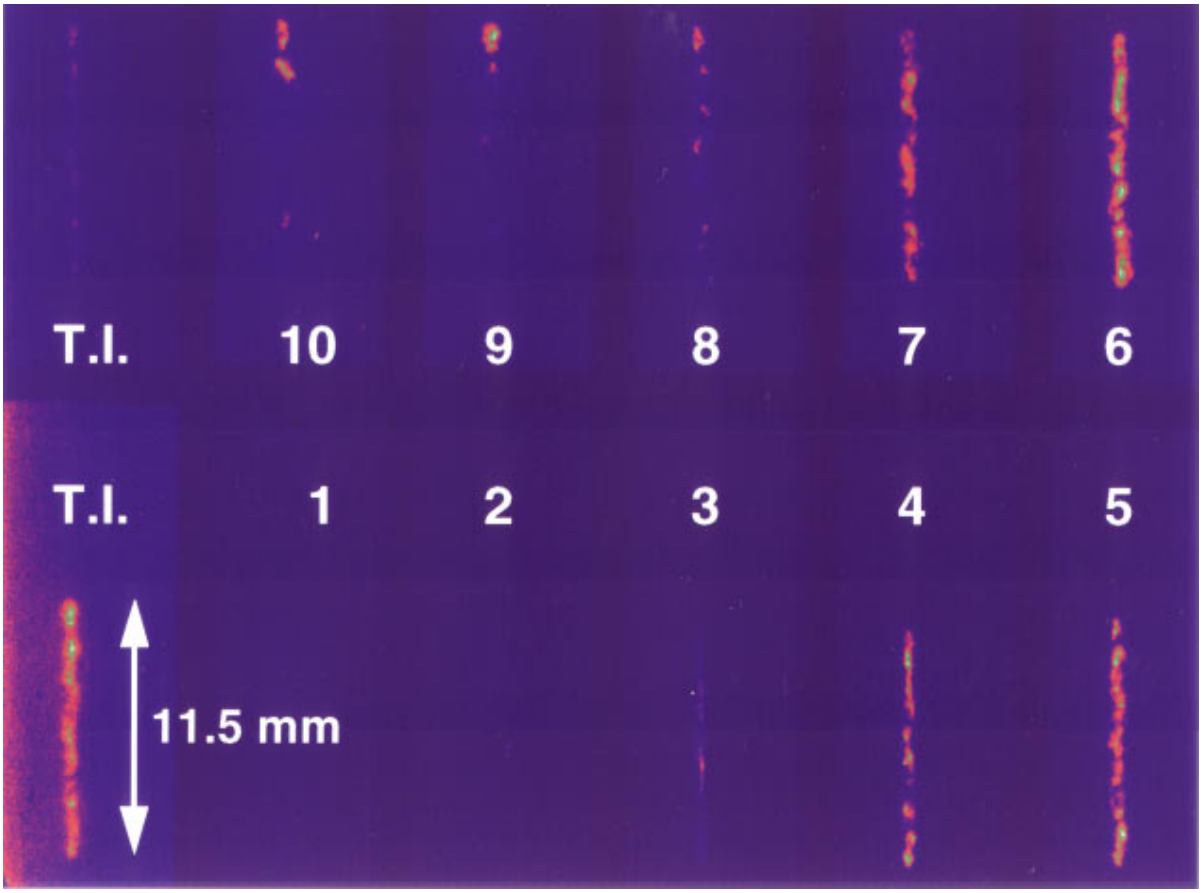

FIG. 7. (Color) An example of the standard format (>800-eV, 2-ns, 250-μm) pinhole camera images for a 40-wire array implosion. This camera is filtered with 8.5 μm of beryllium.

mity so that there has to be some cross coupling (i.e., 3D effects) between the variations in uniformity or wire size and the level of axial uniformity. Increasing the initial wire number from 24 to 70 at this diameter reduced the interwire gap spacing from 1.6 to 0.56 mm. In addition, the wire size was reduced from 13 to 7.5 μm, thus increasing the ratio of the skin depth to the wire size. This will cause the wires to be heated more uniformly; as the wires are more uniformly heated, the $m=0$ instability necks and flares that are prevalent in exploding wires [28–30] are less likely to occur. This in turn may translate into improved axial uniformity because a decrease in these explosion instabilities will likely reduce the seeding of the r-z implosion instabilities like the mag-

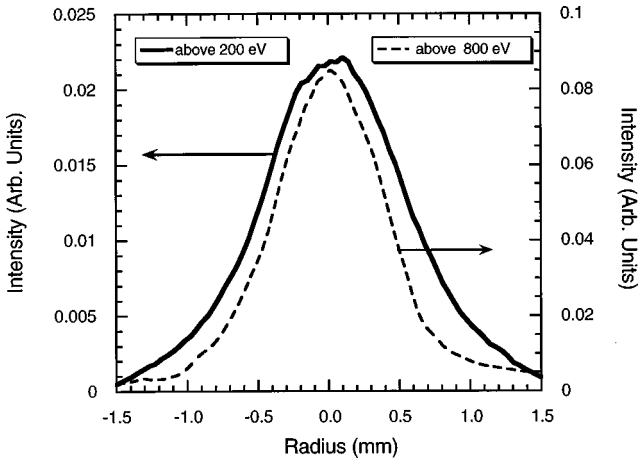

FIG. 8. A comparison of the measured radial profile of the >200-eV and >800-eV emissions as determined from data from the two pinhole cameras. These data are for a 40-wire array. The FWHM of the higher-energy emissions is less than for the softer emissions.

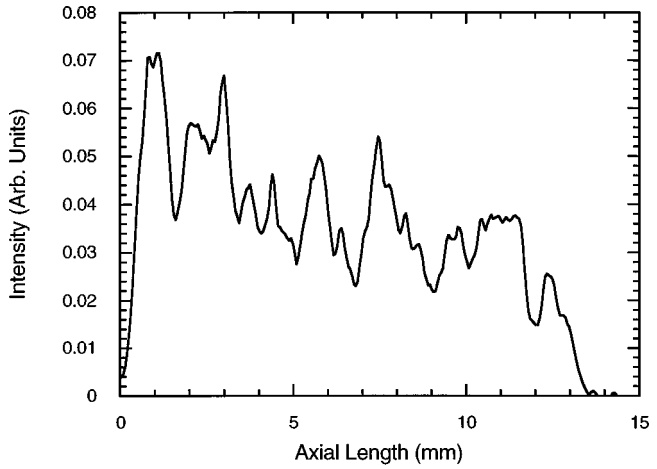

FIG. 9. The axial variation in intensity versus length, as measured at peak power, from the standard-format pinhole camera for a 40-wire array implosion. Using these radially integrated lineouts, an average intensity, hence average variation in intensity, can be calculated. The cathode is at length $z=0$.

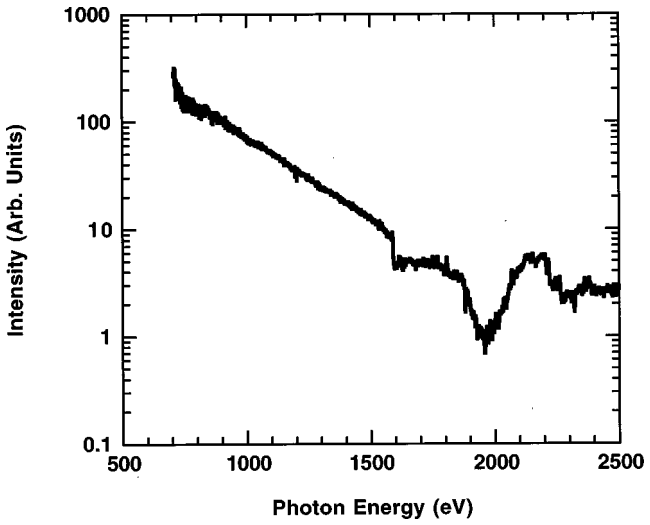

FIG. 10. An example of a measured time-integrated tungsten spectrum for a 12.5-mm-diam, 40-wire array. The small edge is due to the aluminum on the 4-μm Kimfol filter. The slope of the continuum between 800 and 1500 eV corresponds to an electron temperature of 300 eV.

netically driven Rayleigh-Taylor (RT) instability. Aivazov *et al.* [31] have clearly observed axial nonuniformities in wire array implosions due to nonuniform streaming of mass from the unstable explosion of the individual wires. This will be discussed further in Sec. VI.

V. TUNGSTEN RADIUS SCAN

Many experiments have used the radius scaling technique to study the optimization of *K*- and *L*-shell radiators such as neon, aluminum, argon, and nickel [14–16]. By holding the implosion time constant, as the load is moved to increased radius, the mass has to decrease so that in the final plasma state the temperature should increase but the density should fall for a constant final pinch diameter. These trends were measured spectroscopically for *K*-shell radiators; with high-*Z*, broadband radiators, the question is what would happen to the radiated powers and yields with changes in mass and implosion velocity.

Table I lists the three initial load conditions tested in this radius scaling experiment. By increasing the load diameter from 7 to 17.5 mm, the implosion velocity is increased from 28 to 65 cm/μs and the mass is decreased from 2018 to 450 μg/cm. To remove one variable, we increased the wire number as the load diameter increased to maintain a fairly constant wire-to-wire gap. However, this does result in relatively thick (18-μm) wires at the smallest diameter, which could perturb the explosion phase, since the ratio of wire thickness to current skin depth is increased. As discussed in Ref. [32], this can cause the explosion phase (initiation) and implosion phase to occur at the same time, which may have an adverse effect on pinch dynamics.

Figure 14 shows the comparison of total currents, feed currents, and x-ray powers measured for the three-load conditions. The feed currents were fairly close and the implosion times were nearly constant: 48 ± 3 ns. The total radiated energies were similar for the 12.5- and 17.5-mm arrays but it was lower for the 7-mm array. This is may be due to the reduced compression ratio (4:1) produced by such a small initial diameter load which gives less kinetic energy. From Fig. 14 and Table I, it is seen that as the diameter (and collapse velocity) increases, the power increases. The highest collapse velocity (65 cm/μs) load produced a very large x-ray power of 85 TW as measured by the four-channel x-ray diode array. This data suggests that the pulse width is inversely proportional to the collapse velocity squared. This strong function of velocity indicates that the pulse width is

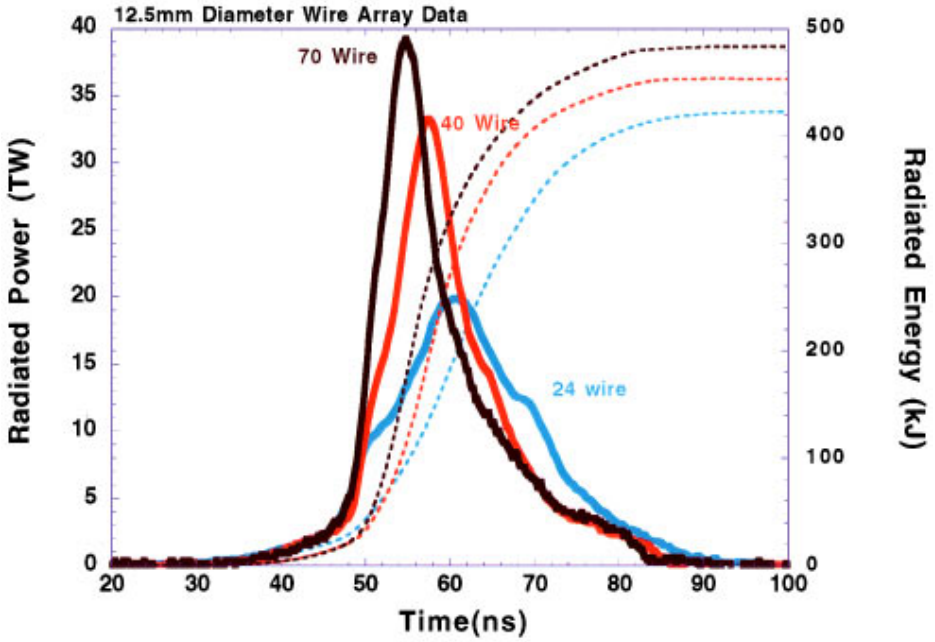

FIG. 11. (Color) Increasing wire number from 24 to 70 increases the power to nearly 40 TW from 12.5-mm arrays with a constant mass of 610 μg/cm. The total radiated energies were 450 ± 30 kJ. The results of all the shots in the wire-number scan are listed in Table II. As the wire number increases, the start of the x-ray pulse does not vary but the peak moves earlier in time.

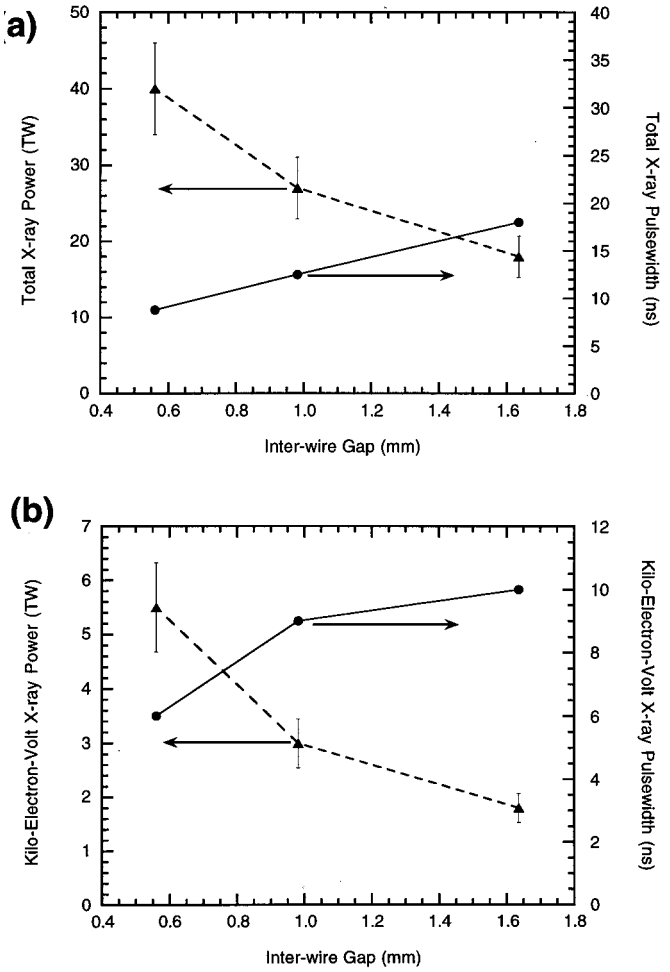

FIG. 12. Wire-number scan shows both increasing (a) total and (b) keV (>800 eV) powers as the gap between wires decreases (i.e., wire number increases) and the wire thickness decreases. The powers are joined with a dashed line and the pulse widths are joined with solid lines in both figures. The >800-eV emission powers increase faster than those for the total (see Fig. 13). The trends in powers agree with the trends in the pulse widths of the signals.

not easily determined by the thermalization time of kinetic energy as defined by Hussey *et al.* [33], which gives an inverse linear scaling. For these cases, if we assume that the imploding sheath thickness is 0.5–0.6 mm (i.e., equivalent to the final pinch radius), the thermalization times would be in the range of 1–2 ns, less than the measured 4–20-ns pulse widths. In addition, the wire thickness may be causing changes in the explosion time of the individual wires, which could be folded into any velocity effects. A systematic experiment where only the wire size is changed and the charge voltage is adjusted to maintain a constant implosion time would aid in understanding the effect of wire size.

The power results are also very reproducible as shown in Fig. 15, which shows the overlay of three consecutive shots. For these shots, an 11-channel x-ray diode array was employed to measure the powers through an aperture that limited the field of view to a 4-mm length of the pinch. Figure 16 shows a comparison of the unfolded spectra for both the 4- and 11-channel instruments. The unfolds do not agree in the details of the spectral shape; however, they both show significant increases in the higher-energy emissions compared to the 12.5-mm-diam wire array data (Fig. 12).

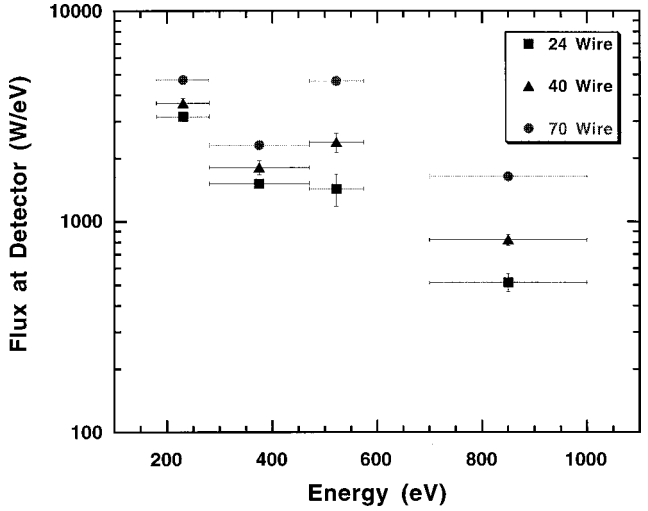

FIG. 13. Plot of the x-ray powers incident on the XRD array. The increased wire number enhances the radiated power, relatively more in the higher-energy channels.

The calibrated 11-channel XRD array gave a somewhat lower power estimate of 65 TW. However, this instrument only viewed a short length of the pinch, which could result in some disagreement due to axial variations in emissions from the pinch. For the purposes of this paper, we therefore report the power to be 75 ± 10 TW. The possible measurement error is larger than the 5% variation in signals over the three shots. This 75 TW represents a power gain of between 3 and 4 over the electrical power of the generator.

VI. TWO-DIMENSIONAL RADIATION—MHD MODELING

To address the variation of the implosion quality and radiated powers with wire number and velocity, we have employed a two-dimensional (r-z) Eulerian code. Ideally, a three-dimensional, detailed radiation—MHD code with appropriate ''cold-start'' models would be able to calculate these dynamics, but such a capability does not exist at present.

In these 2D r-Z calculations, an initial random density perturbation is imposed on a 1-mm-thick plasma shell very early in the dynamical development of the pinch (at the point where the pinch has traveled 2% of the distance to the axis from the original array radius). This annulus is imploded self-consistently. Although most of the changes discussed above occurred in the r-θ plane, we can use the r-z code to assess the magnitude of Rayleigh-Taylor instabilities necessary to simulate the experimental behavior, to understand the pinch energetics, and to estimate what changes may be occurring in the plasma parameters. Moreover, in a Z pinch, r-θ instabilities will grow at a much slower rate than r-z instabilities due to the current being able to redistribute.

Using a seed for RT instabilities to mimic the changes with wire number is not without physical justification since (a) the time-resolved pinhole images showed significant axial variations in emission even at stagnation (see Fig. 17), and (b) the explosion phase of wires is known to be unstable, as previously observed in exploding single wires [28–30,34] and in laser diagnostics of arrays by Aivazov *et al.* [31] The

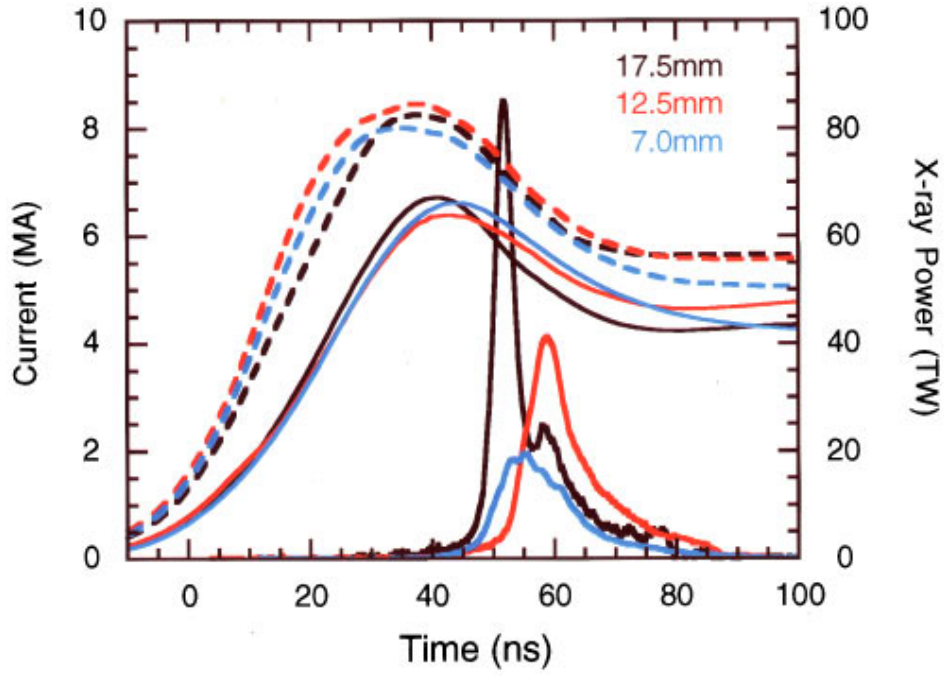

FIG. 14. (Color) Radius scan with approximately constant wire separation shows a strong power dependence with initial diameter. The parameters for these shots are listed in Table I. The change in emission power could be due to dependence on collapse velocity and/or wire thickness.

unstable explosion of the wires will cause random axial mass distributions that will seed the growth of r-z instabilities during the implosion. Remember that as the wire number is increased the wire sizes are reduced so that they are more likely to explode uniformly. More direct evidence of this comes from laser shadowgraphy [35] which shows that in the 120-wire case, the individual wires are expanding and are still descrete up to 25–30 ns into the main current pulse when they merge. This is about the same time that they should begin to move inwards. The wire shadows are rela-

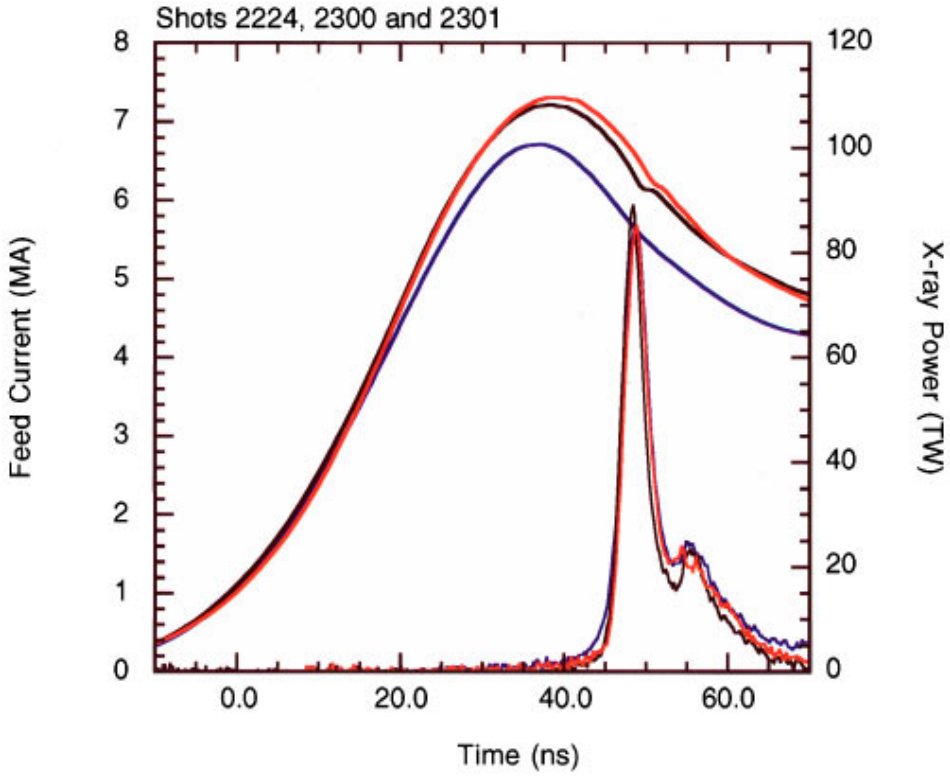

FIG. 15. (Color) The 120-tungsten-wire arrays give very reproducible results. This plot shows three shots 2224, 2300, and 2301. The peak x-ray power varies by less than 5%. The surface brightness temperature is approximately 180 eV.

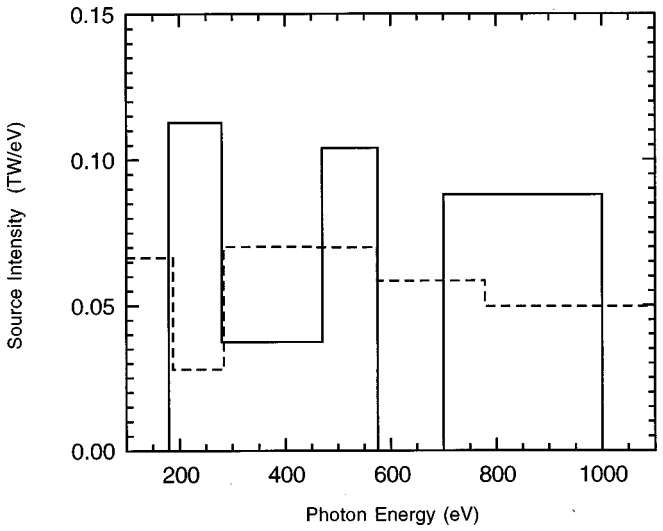

FIG. 16. Comparison of the unfolded spectrum from a four-channel XRD array (solid black line), and an unfolded spectrum from an 11-channel XRD array (blue dashed curve) for a 17.5-mm implosion. Although the spectral shapes do not agree, both sets of measurements do show that the >600-eV emissions have been enhanced compared to the 12.5-mm-diam implosions. This is consistent with an increased temperature due to the higher collapse velocities.

tively uniform; unfortunately, similar measurements were not taken on Saturn with fewer, thicker wires, but data from Aivazov *et al.* [31] show that these types of explosions are unstable.

This argument is in contrast to those discussed in Refs. [9, 36], where the importance of wire number is based on the azimuthal symmetry of the array as it collapses, the merging of the wires to form a shell, and the possibility of angular momentum causing limited compression. However, the last

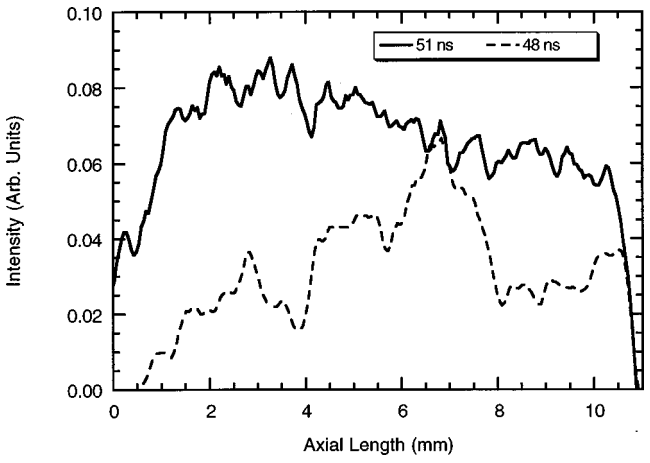

FIG. 17. Axial variation in intensity versus length, as measured at the first strike (i.e., the onset of x-ray emission) and at peak power, from the large-format, >200-eV pinhole camera for a 120-wire, 17.5-mm array implosion. The emission at the first strike is very axially nonuniform, which is consistent with the presence of Rayleigh-Taylor instabilities. The axial nonuniformities have spatial wavelengths of 0.3–2 mm. Near peak power, where the 2D radiation—MHD calculations would suggest that the bulk of the mass has reached the axis, the emission has become more uniform.

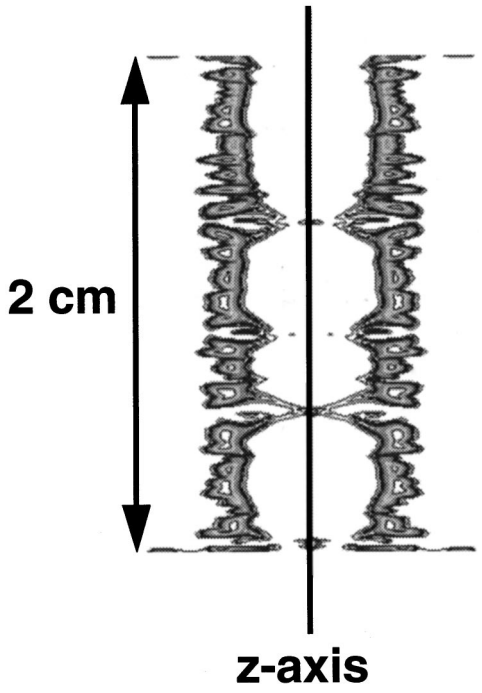

FIG. 18. An example of a 2D calculation with a 15% random-density perturbation (12.5-mm-diam, 70-wire array) 5 ns prior to stagnation. The RT instabilities have wavelengths of 0.8 ± 0.2 mm and they are nonlinear. These instabilities broaden the sheath, thus affecting the pulse width. Instabilities cause the mass to reach the axis early due to blow-in at bubbles and they cause pdV heating of the shell and final pinch.

two hypotheses would explain the reduction in the pinch diameter but not necessarily the observed increase in axial uniformity (see the axial variations listed in Table II).

This 2D code uses the SESAME equation-of-state tables and it is coupled to an equivalent circuit model of the Saturn generator. The radiation transport technique employed is three-temperature (3T) diffusion [37]. This is a reasonable approximation for these tungsten pinches for photon energies where the optical depths [see Figure 3(b)] are greater than 1 over most of the spectrum.

Figure 18 depicts a 2D calculation with an initial 15% perturbation some 5 ns prior to stagnation. The RT instabilities are far into nonlinear development with wavelengths of 0.8 ± 0.2 mm. These instabilities broaden the sheath and send material to the axis early in bubble regions, thus determining the pulse width.

In Fig. 19(a), we show the calculated current and x-ray power pulses for a 610-μg/cm, 12.5-mm-diam, 40-wire array load overlaid with the measured pulses. The calculation used a 30% random-density perturbation. Experiment and calculation agree relatively well in the emission power, the pulse width, and the implosion time. Note that the predicted current falls more quickly and to a lower value than the measured current. This may be due to either the current monitor becoming unreliable after the implosion or the fact that in the experiment there could be a shortening of the MITLs at the convolute so that the current will hold up. The same effect is seen in Fig. 19(b) for a 15% random-density perturbation.

Calculations for the 17.5-mm-diam experiment using a 5% random-density perturbation are shown in Fig. 20 (the

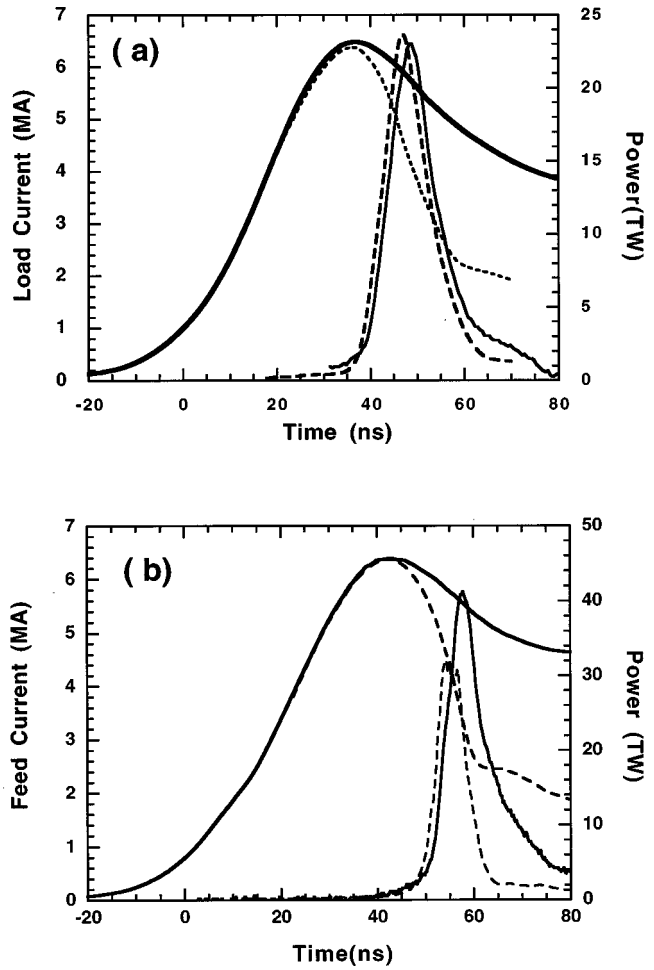

FIG. 19. Comparison of the measured current and x-ray power pulse (solid) and the calculated current and power waveforms (dashed) for (a) a 40-wire, 12.5-mm-diam, 610-μg/cm array (shot 2038) implosion and (b) a 70-wire (shot 2217) implosion. The calculation assumed a 1-mm-thick shell with a 30% random-density perturbation for (a) and a 15% random-density variation for (b). The calculated currents clearly show implosion dips, whereas the experimental data do not. The calculated pulse widths and powers compare well to the measured values, although the calculation for shot 2217 is some 20% low in the power estimate.

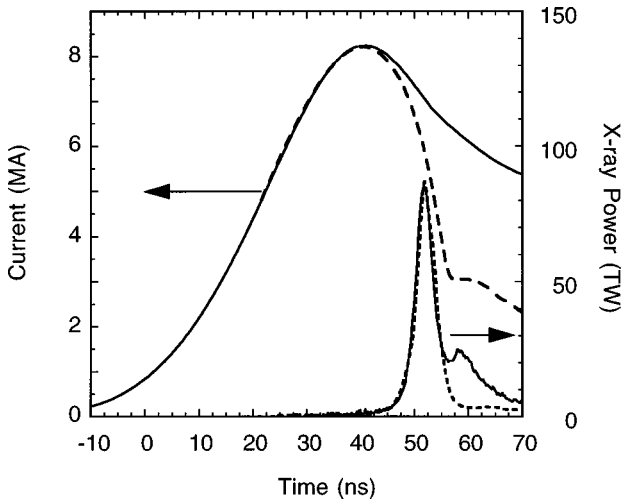

FIG. 20. Comparison of the measured current and x-ray power pulse (solid curves) with the calculated (dashed curves) current and power pulses for a 120-wire, 17.5-mm-diam, 450-μm/cm array (shot 2224). The calculation assumed a 1-mm-thick shell with a 5% random-density perturbation. The pulse width is reduced to 4 ns. The calculation does not reproduce the late-time behavior. The calculated x-ray power is shifted 1 ns. The timebase has $t=0$ equal to the start of the equivalent voltage waveform used to drive the circuit model; this is 37 ns before the extrapolated zero of the current pulse.

time scale is measured from the start of the voltage waveform used in the circuit model). In this case, the calculated powers and pulse widths agree reasonably well with the experiment. The late time emission behavior, when the pinhole cameras (see Figs. 6 and 7) show highly unstable and localized regions, is not well modeled even by this 2D code. These calculations indicate that the collapsing energy is well thermalized; 1–3-keV ion temperatures after stagnation compared to $>$200-keV ions in the collapse. These ion temperatures are consistent with the plasma re-expansion velocities, as measured by the time-resolved pinhole cameras, of about 5–8 cm/μs. We can also surmise that the trends in emissions, as the wire number and collapse velocity were varied, can be represented by r-z calculations, where the seeding for RT instabilities is decreased as the wire number increases and the wire thickness decreases. Comparison of the three different load conditions and calculations is shown in Table III.

In Fig. 21, we show the plot of the average plasma radius and the fraction of the shell mass involved in the instability growth as a function of time. This involved mass is determined by calculating the average density of the shell and then by adding up cell by cell the difference between the cell density and the average (e.g., lower density cells are usually in the bubbles and higher density cells are in the spikes). These absolute differences are converted to mass and then

TABLE III. Comparison between the two-dimensional calculations and some of the wire array shots. The trends in the power and pulse width are consistent with the trends in the calculation as the initial random-density perturbation is decreased.

Wire no.	Diam. (mm)	Mass (μg/cm)	Gap (mm)	Wire thickness (μm)	Pulse FWHM (ns)	Total radiated power (TW)	Random density perturbation (%)	Calculated radiated power (TW)	Calc. FWHM (ns)
40	12.5	610	0.98	10	12$\pm$2	27$\pm$3	30	23	10
70	12.5	610	0.56	7.5	8.5	40	15	32	9
120	17.5	450	0.46	5	3.8$\pm$0.2	75$\pm$10	5	85	4

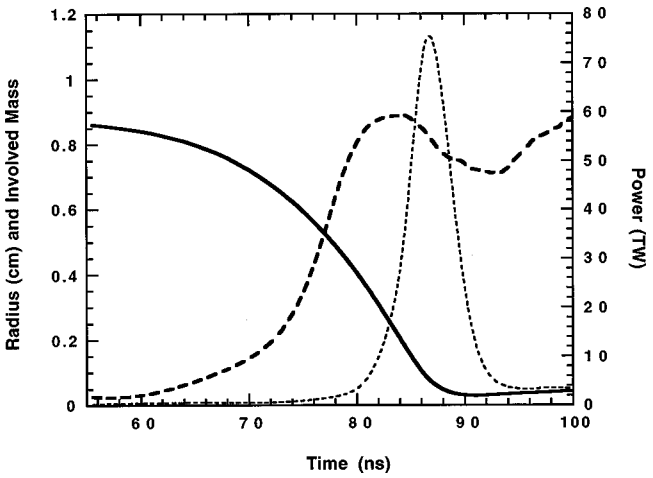

FIG. 21. Calculated average radius (solid curve) and fraction of the mass involved in the unstable shell region (dashed curve) are shown vs time for shot 2224 (see Fig. 20). For reference, the predicted power is shown as a dotted curve. The predicted pinch diameter at a peak power of 1 mm compares well with the measured value of 1.1 ± 0.1 mm as determined from the large-format pinhole camera.

normalized to the initial shell mass. An involved mass of zero therefore corresponds to a perfectly uniform shell and an involved mass of one corresponds to a completely unstable and broken-up shell. For reference in Fig. 21, the predicted power pulse is shown. The predicted average diameter at the time of peak power is 1 mm, which compares to the measured value of 1.1 ± 0.1 mm as determined from the large-format pinhole camera images. The involved mass curve shows a very interesting feature of these implosions with large numbers of thin wires in that as the shell implodes, the mass involved grows as expected due to Rayleigh-Taylor development and the density contour plots show that the RT structure has wavelengths of less than 1 mm. These short wavelengths do break through (the onset of the x-rays in Fig. 21) but the current stays predominantly in the shell, hence the mass involved stops growing just prior to stagnation. It is this lack of long wavelength breakthrough that gives the tight assembly and high radiated powers. In the case shown for the 40 wires at 12.5-mm diam, the initial perturbation level of 30% caused the short wavelengths to saturate very early in the implosion and hence the more destructive longer wavelengths (i.e., $>=2$ mm) had longer to grow so they broke through during the implosion, thus sending mass to the axis early, which significantly broadened the radiation pulse.

Based on these calculations, the increased power in the case of the 17.5-mm implosions may be plausibly attributed to two effects: (1) the thinner wires required a smaller initial random-density perturbation, which produced less spread in the imploding mass resulting in a more rapid thermalization; and (2) the higher collapse velocity caused the peak electron temperature to increase from 160 eV in the 12.5-mm implosions to 250-eV in the 17.5-mm case. The higher electron temperature resulted in a higher brightness temperature.

The two-dimensional calculations also give insight into the heating mechanisms. In 2D, the RT growth causes a net reduction in the peak radial kinetic energy as determined by the 0D slug model coupled to the circuit code; typical 2D peak kinetic energies are <160 kJ in the 17.5-mm-diam load case. However, these calculations have the current flowing after the stagnation, and if the work done on the plasma by the $J \times B$ forces are calculated, this accounts for about 350–400 kJ, which, together with Ohmic heating, explains the measured radiated yield. This work by the magnetic field can enter into kinetic energy (especially during the collapse), pdV work, or shock heating; in all cases, though, these high-Z plasmas are extremely efficient at radiating this energy. Riley *et al.* [34] have suggested that turbulent heating at $m=0$ necks due to the $J \times B$ forces can give significant heating rates. In these tungsten pinches, the sound transit times are 8–16 ns for the 17.5- and 12.5-mm implosions, respectively. The radiation FWHMs are 4 and 8.5 in these same two cases, so it is unlikely that classical $m=0$ instabilities are contributing on the time scales of the peak radiation pulses. Also, the drift parameters are less than 0.1, so anomalous Ohmic heating is unlikely. The actual method by which the plasmas are heated by the $J \times B$ forces will be discussed in a future publication [38].

These comparisons are a first step in understanding these high-atomic-number Z-pinch implosions. Comparing only powers and pulse widths is not sufficient; there have to be more diagnostics. In Refs. [37,39], the authors compared calculations to early-time optical images; our next step is to compare the calculations to our time-resolved pinhole camera images; however, drawing a conclusive tie between early-time wire explosions and seeding RT instabilities will require laser-interferometery and optical-emission diagnostics, as well as the pinch x-ray diagnostics. In the future, we will test spectroscopic dopants to allow direct measurement of the temperatures and densities, as has been performed for other elements [5–7,11–19].

VII. CONCLUSIONS AND FUTURE WORK

In summary, the following conclusions can be drawn from the data.

(1) Increasing the wire number for a given array diameter and for a constant mass increases the radiated power from tungsten Z pinches, with an associated increase in axial uniformity and an increased compression ratio.

(2) Increasing the collapse velocity of tungsten Z pinches produces higher powers with decreased pulse widths from pinches with increased compression ratio.

(3) The total radiated energy from tungsten Z pinches exceeds the kinetic energy by more than a factor of 2.

(4) This non-radial-kinetic heating can occur over a very short time scale, i.e., 4 ns, and it is due to the work done on the plasma by the magnetic field.

(5) Two-dimensional (r-z) radiation-hydrodynamic calculations can reproduce the trends in the data by varying the amplitude of the prescribed initial random-density perturbation.

These data are a first step in increasing the database for high-Z radiators in high-current Z-pinch implosions. Future work will aim at studying the final pinch parameters in

greater detail by employing lower-Z K-shell radiating elements to give spectroscopic information. In addition, the wire-number scaling can be studied using an easier-to-diagnose element such as aluminum; an effort to perform such measurements in continuing. Further increases in radiated power may be possible by moving to higher currents (e.g., the 20-MA PBFA Z generator [18]), by mixing elements, and by developing doped foam annular loads and foils to improve the initial load symmetry.

Based on the present results and scaling them empirically and with the two-dimensional calculations to PBFA Z, the output from this 20-MA generator should exceed 150 TW, which creates many applications for radiation physics, vacuum hohlraums, and x-ray-driven inertial-confinement fusion.

ACKNOWLEDGMENTS

None of this work would have been possible without the excellent technical support of the Saturn crew. The authors would like to acknowledge useful technical discussions with Jack Davis and Ken Whitney of NRL, Paul Springer, Art Toor, Al Osterheld, Chris Keane, and Jim Hammer of LLNL, Tom Sanford of SNL, and Y. Maron of the Weizmann Institute. This work was supported by the US DOE under Contract Number DE-AC04-94 AL85000 and by Gerry Yonas, Don Cook, Jim Powell, and Jeff Quintenz.

[1] N. R. Pereira and J. Davis, J. Appl. Phys. **64**, R1 (1988).

[2] R. B. Spielman, M. K. Matzen, M. A. Palmer, P. B. Rand, T. W. Hussey, and D. H. McDaniel, Appl. Phys. Lett. **47**, 229 (1985).

[3] J. Lindl, Phys. Plasmas **2**, 3933 (1995).

[4] J. P. Apruzese, J. Davis, and K. G. Whitney, J. Appl. Phys. **53**, 4020 (1982).

[5] C. Deeney, T. Nash, R. R. Prasad, L. Warren, and J. P. Apruzese, Appl. Phys. Lett. **58**, 1021 (1991).

[6] J. L. Porter, R. B. Spielman, M. K. Matzen, E. J. McGuire, L. E. Ruggles, M. F. Vargas, J. P. Apruzese, R. W. Clark, and J. Davis, Phys. Rev. Lett. **68**, 796 (1992).

[7] C. Deeney, P. D. LePell, F. L. Cochran, M. C. Coulter, K. G. Whitney, and J. Davis, Phys. Fluids B **5**, 992 (1993).

[8] W. W. Hsing and J. L. Porter, Appl. Phys. Lett. **50**, 1572 (1987).

[9] T. W. L. Sanford, T. J. Nash, B. M. Marder, R. C. Mock, M. R. Douglas, R. B. Spielman, J. F. Seamen, J. S. McGurn, D. O. Jobe, T. L. Gilliland, M. F. Vargas, R. Humphreys, K. W. Struve, W. A. Stygar, J. H. Hammer, J. H. DeGroot, J. S. Eddleman, K. G. Whitney, J. W. Thornhill, P. E. Pulsifer, J. P. Apruzese, D. Mosher, and Y. Maron, in *Proceedings of the 11th International Conference on High Power Particle Beams, Prague, 1996*, edited by P. Sunka, K. Jungwrith, and J. Ullschmied (unpublished); T. W. L. Sanford *et al.*, Phys. Rev. Lett. **77**, 5063 (1996).

[10] D. H. McDaniel and W. Hsing (private communication).

[11] C. Deeney, P. D. LePell, B. H. Failor, S. L. Wong, J. P. Apruzese, K. G. Whitney, J. W. Thornhill, J. Davis, E. Yadlowsky, R. C. Hazelton, J. J. Moschella, T. J. Nash, and N. Loter, Phys. Rev. E **51**, 4823 (1995).

[12] K. G. Whitney, J. W. Thornhill, J. P. Apruzese, and J. Davis, J. Appl. Phys. **67**, 1725 (1990).

[13] J. W. Thornhill, K. G. Whitney, C. Deeney, and P. D. LePell, Phys. Plasmas **1**, 321 (1994).

[14] M. Gersten, W. Clark, J. E. Rauch, G. M. Wilkinson, J. Katzenstein, R. D. Richardson, J. Davis, D. Duston, J. P. Apruzese, and R. Clark, Phys. Rev. A **33**, 477 (1986).

[15] C. Deeney, T. Nash, R. R. Prasad, L. Warren, K. G. Whitney, J. W. Thornhill, and M. C. Coulter, Phys. Rev. A **44**, 6762 (1991).

[16] C. Deeney, T. Nash, P. D. LePell, K. Childers, M. Krishnan, K. G. Whitney, and J. W. Thornhill, J. Quant. Spectrosc. Radiat. Transf. **44**, 457 (1990).

[17] J. C. Riordan, J. S. Pearlman, M. Gersten, and J. E. Rauch, in *Low-energy X-ray Diagnostics*, Proceedings of the Topical Conference on Low-energy X-ray Diagnostics, AIP Conf. Proc. No. 75 edited by David T. Attwood and Burton L. Henke, (AIP, New York, 1981), p. 35.

[18] R. B. Spielman *et al.*, in Proceedings of the 11th International Conference on High Power Particle Beams (Ref. [9]) (unpublished).

[19] R. B. Spielman, R. J. Dukart, D. L. Hanson, B. A. Hammel, W. W. Hsing, M. K. Matzen, and J. L. Porter, in Proceedings of the Second International Conference on Dense Z Pinches, *Laguna Beach, CA, 1989*, edited by N. R. Pereira, J. Davis, and N. Rostoker (AIP, New York, 1989), p3.

[20] V. Smirnov *et al.*, in Proceedings of the Ninth International Conference on High Power Particle Beams, Washington, DC, 1992 (National Technical Information Service, Springfield, VA).

[21] C. W. Mendel, Jr. and S. E. Rosenthal, in Proceedings of the Tenth International Conference on High Power Particle Beams, edited by B. Rix and R. White, San Diego, Ca, 1994 (National Technical Information Service, Springfield, VA).

[22] T. W. L. Sanford *et al.*, Sandia National Laboratory, Report No. SAND96-0222 UC-706 (1996).

[23] R. H. Day, P. Lee, E. B. Saloman, and D. Nagel, J. Appl. Phys. **52**, 6965 (1981).

[24] J. McGurn and G. Chandler (private communication). Information on manufacturing these cathodes can be obtained from J. McGurn, Org. 9573, MS-1194, Sandia National Laboratory, 1515 Eubank Ave. SE, Albuquerque, NM 87185, USA.

[25] P. Wang and J. J. MacFarlane, University of Wisconsin Fusion Technology Institute, Report No. UWFDM-1013 (1996) (unpublished).

[26] T. Nash, C. Deeney, M. Krishnan, R. R. Prasad, P. D. LePell, and L. Warren, J. Quant. Spectrosc. Radiat. Transf. **44**, 485 (1990).

[27] B. H. Failor, C. Deeney, J. Riordan, P. D. LePell, and C. A. Coverdale, Bull. Am. Phys. Soc. **40**, 1846 (1995).

[28] E. J. Yadlowsky, J. J. Moschella, R. C. Hazelton, T. B. Settersten, G. G. Spanjers, C. Deeney, B. H. Failor, J. Davis, J. P. Apruzese, K. G. Whitney, and J. W. Thornhill, Phys. Plasmas **3**, 1745 (1996).

[29] L. E. Aranchuk, S. L. Bogolybskii, G. S. Volkov, V. D. Korolev, Yu V. Koba, V. I. Liskonov, A. A. Lukin, L. B. Nikandrov, O. V. Tel'kovskaya, M. V. Tulupov, A. S. Cherenko, Y. Va Tsarfin, and V. V. Yan'kov, Sov. J. Plasma Phys. **12**, 765 (1986).

[30] G. S. Sarkisov, A. S. Shikanov, B. Etlicher, S. Attelan, and C. Rouille, Pis'ma Zh. Eksp. Teor. Fiz. **61**, 471 (1995) [JETP Lett. **61**, 485 (1995)].

[31] I. K. Aivazov, V. D. Vikarev, G. S. Volkov, L. B. Nikandrov, V. P. Smirnov, and V. Ya Tsarfin, Fiz. Plazmy **14**, 197 (1988) [Sov. J. Plasma Phys. **14**, 110 (1988)].

[32] K. G. Whitney, J. W. Thornhill, R. B. Spielman, T. J. Nash, J. S. McGurn, L. E. Ruggles, and M. C. Coulter, in *Dense Z-Pinches*, edited by Malcolm Haines and Andrew Knight, AIP Conf. Proc. 429.

[33] T. W. Hussey, N. F. Roderick, U. Shumlak, R. B. Spielman, and C. Deeney, Phys. Plasmas **2**, 2055 (1995).

[34] R. Riley, D. Scudder, J. Shlachter, and R. Lovberg, Phys. Plasmas **3**, 1314 (1996).

[35] C. Deeney, J. McGurn, D. Noack, J. L. Porter, R. B. Spielman, J. F. Seamen, D. O. Jobe, M. F. Vargas, T. Gilliland, M. R. Douglas, and M. K. Matzen, Rev. Sci. Instrum. **68**, 653 (1997).

[36] D. Mosher, in Proceedings of the Tenth International Conference on High Power Particle Beams, San Diego, Ca, 1994, edited by B. Rix and R. White (National Technical Information Service, Springfield, VA).

[37] D. L. Peterson, R. L. Bowers, J. H. Brownell, A. E. Greene, K. D. McLenithan, T. A. Oliphant, N. F. Roderick, and A. J. Scannapieco, Phys. Plasmas **3**, 368 (1996).

[38] D. L. Peterson (private communication).

[39] W. Matuska, R. L. Bowers, J. H. Brownell, H. Lee, C. M. Lund, D. L. Peterson, and N. F. Roderick, Phys. Plasmas **3**, 1415 (1996).